Striped, honeycomb, and twisted moiré patterns in surface adsorption systems with highly degenerate commensurate ground states

K. R. Elder,[1] C. V. Achim,[2] E. Granato,[3,4] S. C. Ying,[4] and T. Ala-Nissila[4,5,6]

[1]*Department of Physics, Oakland University, Rochester, Michigan 48309, USA*

[2]*Water Research Center for Agriculture and Mining (CRHIAM), University of Concepción, 4030000 Concepción, Chile*

[3]*Laboratório Associado de Sensores e Materiais, Instituto Nacional de Pesquisas Espaciais,12227-010 São José dos Campos, SP, Brazil*

[4]*Department of Physics, P.O. Box 1843, Brown University, Providence, RI 02912-1843, USA*

[5]*COMP CoE at the Department of Applied Physics, Aalto University School of Science, P.O. Box 11000, FI-00076 Aalto, Espoo, Finland*

[6]*Departments of Mathematical Sciences and Physics, Loughborough University, Loughborough, Leicestershire LE11 3TU, UK*

Atomistically thin adsorbate layers on surfaces with a lattice mismatch display complex spatial patterns and ordering due to strain-driven self-organization. In this work, a general formalism to model such ultrathin adsorption layers that properly takes into account the competition between strain and adhesion energy of the layers is presented. The model is based on the amplitude expansion of the two-dimensional phase field crystal (PFC) model, which retains atomistic length scales but allows relaxation of the layers at diffusive time scales. The specific systems considered here include cases where both the film and the adsorption potential can have either honeycomb (H) or triangular (T) symmetry. These systems include the so-called (1×1), $(\sqrt{3} \times \sqrt{3}) R30°$, (2×2), $(\sqrt{7} \times \sqrt{7}) R19.1°$, and other higher order states that can contain a multitude of degenerate commensurate ground states. The relevant phase diagrams for many combinations of the H and T systems are mapped out as a function of adhesion strength and misfit strain. The coarsening patterns in some of these systems is also examined. The predictions are in good agreement with existing experimental data for selected strained ultrathin adsorption layers.

I. INTRODUCTION

When ultrathin films of just a few atomic layers in thickness are grown on atomically smooth surfaces, there is in general a competition between the strain energy in the film and the adsorption potential energy resulting from the interaction of the adsorbate atoms interacting with the substrate. This competition can lead to commensurate states as well as interesting striped and moiré patterns in the incommensurate states. Understanding and predicting these states and the transition between them has been of great fundamental interest for many years. Most recently there has been considerable work devoted to the study of the growth and properties of two-dimensional (2D) films, in particular graphene [1–11], and other films of honeycomb symmetry such as so-called hexagonal boron nitride or hBN (which actually forms a honeycomb structure) [12–19] and MoS_2 [20–22]. These systems typically show 2D moiré patterns that are defined by a triangular (honeycomb) array of commensurate regions when grown on a substrate with an adsorption surface potential having a triangular (honeycomb) array of minima. More complex patterns emerge in other adsorption systems, for example, when Cu is grown on Ru(0001), in addition to honeycomb patterns, zig-zag, and one-dimensional (1D) stripes can form [23–25]. In this work, additional patterns that resemble twisted honeycombs are predicted to occur in some adsorption systems.

Moiré patterns can emerge in nature in many different circumstances, perhaps the simplest example being when a screen or periodic lattice is overlaid on another with a slightly different periodicity. As illustrated in Fig. 1, patterns emerge even in the absence of coupling between the two screens or layers. More interesting patterns emerge when they are coupled as certain regions will become more energetically favorable and tend to enlarge or even lead to a change in the pattern. In this work, the moiré patterns that emerge when a monolayer experiences an adsorption potential that has a different lattice constant and in some cases also a different symmetry are considered. For a film strained such that adatoms can be at the adsorption potential minima locations, an increase in the strain energy in the film will occur. In contrast, if the film is completely incommensurate and unstrained, most of the adsorbate atoms will be located away from the potential minima. A competition between these two factors leads, in 1D at a small misfit strain, to a second-order phase transition (in the absence of thermal fluctuations) from a commensurate state to an incommensurate "striped" state consisting of a period array of domain walls separating the commensurate regions. This phenomenon can be well described by ball and spring models such as the Frenkel-Kontarova model or by continuous models, such as the sine-Gordon model. The situation is much more complex in higher dimensions where the relative symmetry of the film and substrate will influence the patterns that form and often will lead to 2D moiré patterns.

In this work, the ordering of films of honeycomb (H) or triangular (T) symmetry are considered on substrates where the adsorption potential maxima for the adsorbed atoms have either H or T symmetry. These different classes of adsorption systems will be referred to as HH, HT, TH, and TT, respectively, where the latter letter refers to the substrate symmetry. These classes of systems include adsorption systems such as Cu, Ni, or Co on Ru(0001) [23,26–28], Ni on Rh(111), Co on Pd(111), Cu on Pd(111) [29–31], and Ag on Cu(111) [32–38] or Ni(111) [39], graphene on a wide variety of metallic (111) substrates [1–11], hexagonal boron nitride grown on Ir(111) [12], Cu(111)[13–15], Rh(111)[16–18], and Ru(0001)[19].
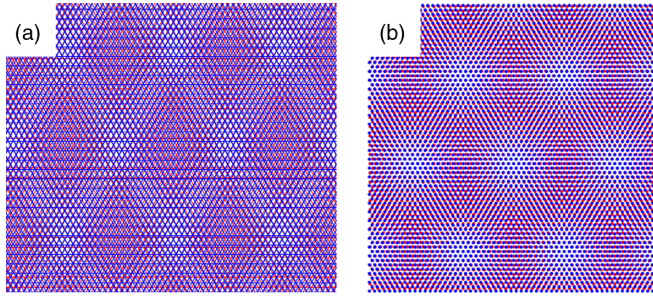
FIG. 1. (a) The characteristic moiré pattern that emerges when a blue triangular mesh or screen is overlaid on a red one that is 5% smaller than that of the blue one. (b) A triangular periodic array of blue points is overlaid on a similar red set that are 5% smaller.

In the systems listed above the natural atomic spacing of the films is close to that of the substrate, leading to a (1×1) commensurate state of the film with the same lattice constant as the substrate. When this is not the case, higher-order commensurate states can occur, which include the $(\sqrt{3} \times \sqrt{3})\,R30°$, (2×2), and $(\sqrt{7} \times \sqrt{7})\,R19.1°$ cases, in which the commensurate state of the film has lattice constants $\sqrt{3}$, 2 and $\sqrt{7}$ times larger, respectively, than that of the substrate and the relative orientation of the film to substrate is $30°$, $0°$, and $19.1°$, respectively. The $(\sqrt{3} \times \sqrt{3})\,R30°$ systems include Xe and Kr on graphite [40,41], Xe on Pt(111) [42], Ag on Si(111) [43], Au on Ge(111) [44], and K on Al(111) [45]. Many other additional cases can be found in the literature. As the atomic spacing of the film atoms increases relative to the substrate, the number of degenerate commensurate states increases leading to more complex pattern.

The purpose of this work is to present a general method for studying the type of atomistically thin films described above and to show how the competition between the elastic and adsorption energies, the relative symmetry of the film and substrate, and the degeneracy of the higher-order commensurate states can influence the patterns that form. The method incorporated here is essentially an extension of the one used in the authors previous studies of (1×1) systems [11,24,25,46] and the $(\sqrt{3} \times \sqrt{3})\,R30°$ system [47]. The method is based on the amplitude expansion [48–53] of the phase field crystal (PFC) model [54–56], which describes a field related to local number density fluctuations. This amplitude expansion approach uses spatially varying complex amplitudes to describe these density fluctuations in the film and models the substrate by a rigid potential. For practical purposes, only the amplitudes of the lowest-order Fourier modes are included in such an approach, which would imply that except for the (1×1) case, the higher-order commensurate states would not couple to the substrate which is unphysical. This problem does not exist in the full PFC model that includes all the Fourier modes. As discussed in Ref. [47] and generalized in this work, the higher-order Fourier modes couple both to the adsorption potential and the lowest order modes. When the higher Fourier modes are integrated out, one obtains nonlinear coupling between the adsorption potential and the lowest order modes. In this work, this result is exploited to develop the simplest possible model that uses the amplitude expansion for only the lowest Fourier modes

to study all the intricate patterns involving the higher order commensurate systems and the transitions between various incommensurate and commensurate states. This is achieved by using an effective nonlinear film substrate coupling involving the lowest power of the density that mimics the full coupling of the density to the substrate. This new amplitude expansion model can be used to study the ordering for a class of systems with all types of commensurate states such as (1×1), $(\sqrt{3} \times \sqrt{3})\,R30°$, (2×2), $(\sqrt{7} \times \sqrt{7})\,R19.1°$, and even higher-order ones.

When the periodic adsorption potential is represented in the simplest form by the lowest order Fourier components, there is also an extra simplification. It is easy to see that by just flipping the sign of the potential one can turn for example a triangular (T) substrate to a honeycomb (H) substrate and vice versa. The same applies to the symmetry of the film. As a result, from the symmetry point of view the ordering of a H film on a T substrate (which will be referred to as a "HT" system in what follows) is identical to a T film on a H substrate (a "TH" system) in this model. Similarly, a HH system is identical to a TT system. Another advantage of the amplitude expansion method is that it can be numerically implemented to study relatively large-scale systems, up to micrometer length scales. The length scale of the patterns diverges in the limit of zero misfit and very large systems are required in this limit. Thus, for the study of the commensurate-incommensurate transition it is essential to have a simple model that can be used to examine large systems, while still retaining atomistic details such as defects. The largest system considered using the amplitude method to date (to the best knowledge of the authors) has been for a 2D film of size 20 μm $\times$ 34 μm containing roughly 25 billion atoms (number density maxima) [46].

In this manuscript, a general methodology is outlined and then used to examine surface ordering in TH and TT systems for the (1×1), $(\sqrt{3} \times \sqrt{3})\,R30°$, (2×2), and $(\sqrt{7} \times \sqrt{7})\,R19.1°$ structures. For completeness, the results for the previously studied case of the TH $(\sqrt{3} \times \sqrt{3})\,R30°$ system will be reported in addition to the HT and TT (2×2) and HT and TT $(\sqrt{7} \times \sqrt{7})\,R19.1°$ systems, which were not previously considered. Phase diagrams are presented for all these systems to highlight the influence of symmetry on the differences and similarities between them. As discussed previously, there exists significant differences between the TH (or HT) and TT (or HH) systems for the (1×1) structure. Not surprisingly, similar differences appear for the higher order structures examined in this work. There is also a noticeable difference between the (1×1) and higher-order structures. This difference is mainly due to the fact that the degenerate commensurate sublattices in the higher-order states are closer together, implying a smaller change in elastic energy when a junction or a domain wall is crossed. The most striking difference occurs in the TT case in which junctions break into dislocation pairs as the film-substrate coupling is increased for the (1×1) case, while the junctions only twist in higher order structures. This feature may be model dependent and more microscopic approaches are needed to determine how generic it is. While some aspects of the patterns that form may be model-dependent, many of the predictions of the work presented here are consistent with many experimental results as discussed in detail in Sec. VI.

The manuscript is organized as follows. In Sec. II the possible commensurate states for a given system are characterized and the degeneracy of the states is determined. In Sec. III the model used to describe these systems is detailed. To make a connection with physical systems the small deformation limit of this model is undertaken in Sec. IV and analytic results are given for the stripe-commensurate transition. Section V presents the results for the phase diagram of all the systems considered here. This is followed by a comparison of the results with experiments and other theoretical works in Sec. VI and a discussion of the limitations of the methodology follows in Sec. VII. Finally, some concluding remarks are made in Sec. VIII.

II. CHARACTERIZATION AND DEGENERACY OF COMMENSURATE STATES

A. Characterization of commensurate states

In this section, the characterization of commensurate states for different combinations of film and adsorption potential symmetries is examined. Consider a commensurate state in which the distance between adatoms is

$$d = \sqrt{\left[(j + 1/2)a_x^s\right]^2 + \left(a_y^s\right)^2}, \qquad (1)$$

where a_x^s and $a_y^s = \sqrt{3}a_x^s/2$ are defined with respect to the substrate lattice constant as shown in Fig. 2(a) and j is an integer [e.g., $j = 3$ in Fig. 2(a)]. There are two sets of sublattices that could be defined as shown in the blue or red set of points in this figure. For the purposes of the present calculations only the red set will be considered. It should also be noted that the two sets overlap for $j = 0$ and 1. The dimensionless length scale L of the commensurate state can be given in terms of j as

$$L(j) = \frac{d}{a_x^s} = \frac{1}{2}\sqrt{(2j + 1)^2 + 3}. \qquad (2)$$

This gives $L(0) = 1$, $L(1) = \sqrt{3}$, $L(2) = \sqrt{7}$, $L(3) = \sqrt{13}$, etc. The angle this line makes with the respect to the
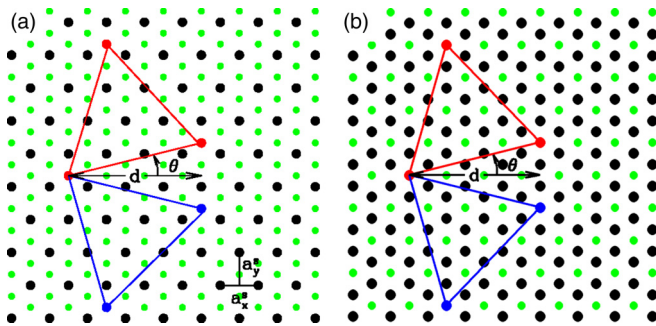

FIG. 2. Schematic of the film-substrate geometry. In these figures the black and green points represent the maxima and minima of the adsorption potential, respectively. For convenience a substrate with a triangular or honeycomb array of maxima will be correspondingly referred to as a triangular (T) and honeycomb (H) substrate. In both figures a unit cell of a commensurate state for the triangular film (T) is shown for the parameters $(j,m) = (3,0)$ (see text for details).
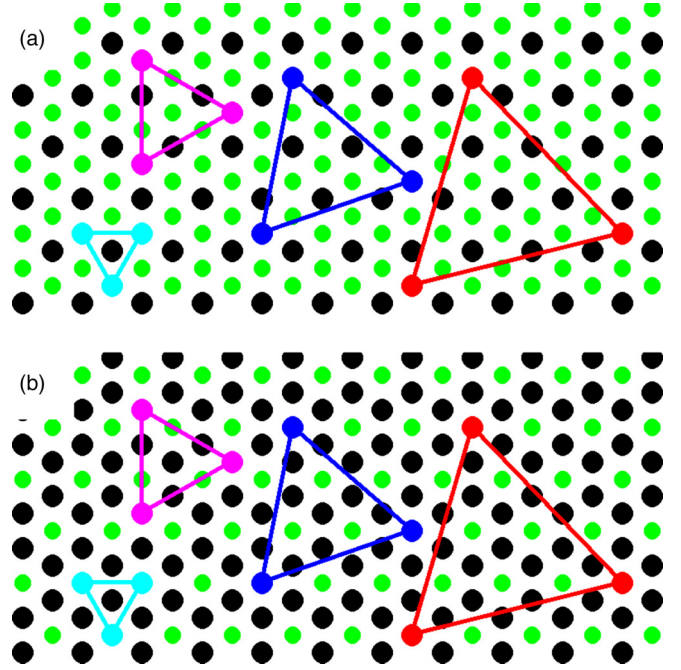

FIG. 3. Sample commensurate unit cells are shown in (a) and (b) for the TT and TH systems, respectively. In these figures $m = 1$ and $j = 0, 1, 2$, and 3 for the cyan, purple, blue, and red lines and points, respectively.

horizontal is

$$\theta(j) = \pm \tan^{-1}\left(\frac{\sqrt{3}}{2j + 1}\right). \qquad (3)$$

The $\pm$ correspond to the two equivalent sets of sublattices. For simplicity in what follows the $+$ set of states will be considered.

In Fig. 2 the $j = 3$ states are illustrated for both the TT and TH systems. As discussed in the Introduction it is important to note that in the simple model used here, the relative symmetry of the TH system is equivalent to that of the HT system. Thus, the results obtained for the TH system are also applicable to, for example, graphene adsorbed on various compact fcc(111) surfaces. It should be noted that the distance between nearest-neighbor surface atoms is $d/\sqrt{3}$ for the HT system. Similarly a HH system is equivalent to a TT system. Samples of the various unit cells for the TT and TH systems are illustrated in Figs. 3(a) and 3(b), respectively, for $j = 0, 1, 2$, and 3.
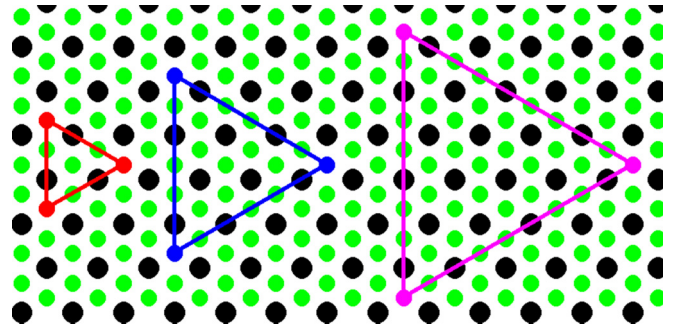

FIG. 4. Sample commensurate unit cells for the TT system with $j = 1$ and $m = 1, 2$, and 3 in red, blue, and purple, respectively.
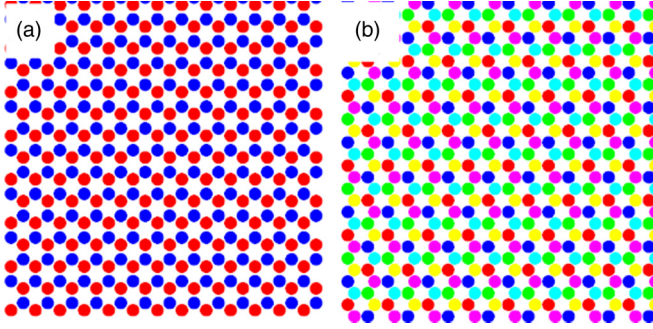
FIG. 5. Sample commensurate states for the TT system with $m = 1$ for $j = 0$ and 1 in (a) and (b), respectively. Each color represents a different degenerate commensurate state.

It is also useful to note that adatoms located at integer multiple number of d at the same angle θ, implying structures with lattice constants,

$$d(j,m) = \frac{m}{2}(\sqrt{(2j+1)^2 + 3})a_x^s, \quad (4)$$

where m is an integer would also form commensurate states. Some samples or ordered structures are shown for $j = 1$ and various m in Fig. 4 for the TT system.

B. Degeneracy of commensurate states

Depending on the integers j and m there can be many equivalent commensurate states. For example for $(j,m) = (0,1)$ there are two equivalent commensurate states for the TT case and one for the TH case. As j and m increase the number of equivalent commensurate states increases. The number N of such sublattices is

$$N = \begin{cases} (mL)^2 = m^2[(2j+1)^2 + 3]/4, & \text{for TH;} \\ 2(mL)^2 = m^2[(2j+1)^2 + 3]/2, & \text{for TT.} \end{cases} \quad (5)$$

Sample sets of commensurate states are shown in Figs. 5 and 6 for the TT and TH systems, respectively. In the TT case there are N additional states for $j > 1$ due to the rotation by $-\theta$.

Table I summarizes the classification and degeneracy of the different commensurate states for several representative values of j and m.
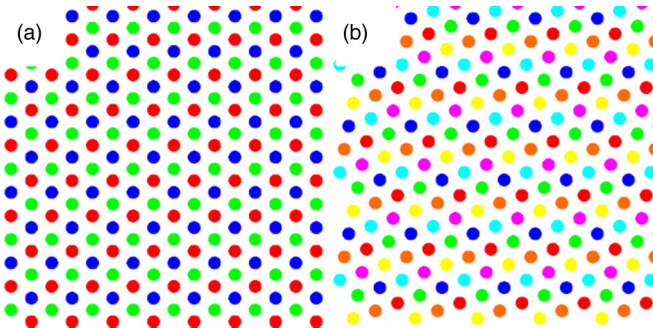

FIG. 6. Sample commensurate states for the TH system with $m = 1$ for $j = 1$ and 2 in (a) and (b), respectively. Each color represents a different degenerate commensurate state. It should be noted that in the $(j,m) = (0,1)$ there is only one commensurate state.

TABLE I. Table outlining the structures corresponding to the sublattices with different j and m for the commensurate states in the TH system. The number of sublattices (N) is twice as large for the TT system.

j	m	L	N_{TH}	θ	Phase
0	1	1	1	60°	1×1
0	2	2	4	60°	2×2
1	1	$\sqrt{3}$	3	30°	$(\sqrt{3} \times \sqrt{3})$ 30°
1	2	$2\sqrt{3}$	12	30°	$(2\sqrt{3} \times 2\sqrt{3})$ R30°
2	1	$\sqrt{7}$	7	19.1°	$(\sqrt{7} \times \sqrt{7})$R19.1°
2	2	$2\sqrt{7}$	28	19.1°	$(2\sqrt{7} \times 2\sqrt{7})$R19.1°
3	1	$\sqrt{13}$	13	13.9°	$(\sqrt{13} \times \sqrt{13})$ R13.9°
3	2	$2\sqrt{13}$	52	13.9°	$(2\sqrt{13} \times 2\sqrt{13})$ R13.9°
4	1	$\sqrt{21}$	21	10.9°	$(\sqrt{21} \times \sqrt{21})$ R10.9°
4	2	$2\sqrt{21}$	84	10.9°	$(2\sqrt{21} \times 2\sqrt{21})$ R10.9°

III. MODEL

Ideally a fully atomistic method such as molecular dynamics (MD) or even quantum mechanical density functional theory would be employed to study the structure and energetics of ordering and patterns of surface adsorbates. Unfortunately, only a few hundred or at best a few thousand atoms can be handled fully quantum mechanically and even the classical MD method is numerically restricted by atomic length scales and phonon vibrational time scales. The phase field crystal (PFC) method [54–57] on the other hand can access much larger (diffusive) time scales and can be used to find equilibrium patterns much more rapidly. However, the PFC method resolves features at atomic scales, which is still somewhat restrictive in terms of the computational effort. Typically, the size of the adsorbate patterns scales as the inverse of the misfit strain for small film-substrate couplings and can diverge near the commensurate-incommensurate phase transitions (in the mean field limit). For this reason it is imperative to consider the amplitude expansion of the phase field crystal model [48–53] (APFC), which is described in detail below. This approach is particularly useful for systems where deviations from a single orientation are minor. It makes it relatively simple to construct phase diagrams of surface ordering, since the films are often of a single orientation, with some small deviations near domain walls and their junctions, and the complex amplitudes that enter the approach are very uniform allowing for relatively large grid spacings in the numerical implementation of the APFC model.

To describe this approach it is useful to consider the original 2D PFC model in the presence of an adsorption potential $V(\vec{r})$. The dimensionless PFC free energy $\mathcal{F}$ can be written as a functional of the atomic number density field n as follows:

$$\mathcal{F} = \int d\vec{r}\left[\frac{\Delta B}{2}n^2 + \frac{B^x}{2}n(1+\nabla^2)^2n - \frac{\tau}{3}n^3 + \frac{v}{4}n^4 + Vn\right]. \quad (6)$$

The various parameters that enter this description have been discussed in detail in prior works [54–57]. The part of the free energy without the adsorption potential is minimized by a triangular pattern of density field maxima for $\tau > 0$ and a

honeycomb pattern of density field maxima for $\tau < 0$. In the APFC method, a set of complex amplitudes η_{kl} are used to describe the dimensionless number density field n. For films of triangular and honeycomb symmetry it is convenient to expand n as

$$n = \sum \eta_{kl} e^{i\alpha \vec{G}_{kl}^{f} \cdot \vec{r}} + \text{c.c.}, \qquad (7)$$

where c.c. is the complex conjugate, $\vec{G}_{kl}^{f} = k\vec{q}_1 + l\vec{q}_2$, $\vec{q}_1 = (-\sqrt{3}, -1)/2$, and $\vec{q}_2 = (0,1)$. The parameter $\alpha = 1 - \varepsilon$ is related to the misfit strain ε defined as $\varepsilon = (a^s - a)/a^s$, where a is the natural lattice constant of the adsorbate film, and a^s is the lattice constant of the substrate. In this formulation the complex amplitudes, η_{kl}, are expanded around the lattice constant of the substrate, implying that they are constant in a perfect commensurate state and vary periodically in a perfect incommensurate state. In the incommensurate state the lattice constant of the film is exactly $a_x = 4\pi/\sqrt{3}$ when $V = 0$.

For simplicity the interaction with the substrate will be modeled by a rigid adsorption potential V described in a similar fashion, i.e.,

$$V = V_0 \sum_{kl} e^{i\vec{G}_{kl}^{s} \cdot \vec{r}} + \text{c.c.}, \qquad (8)$$

and

$$\begin{aligned}
\left(\vec{G}_{kl}^{s}\right)_x &= \alpha L\left[\left(G_{kl}^{f}\right)_x \cos\theta - \left(G_{kl}^{f}\right)_y \sin\theta\right], \\
\left(\vec{G}_{kl}^{s}\right)_y &= \alpha L\left[\left(G_{kl}^{f}\right)_x \sin\theta + \left(G_{kl}^{f}\right)_y \cos\theta\right],
\end{aligned} \qquad (9)$$

and the same modes (kl) used for the film are used for the substrate, and L and θ are the dimensionless length and angle described by Eqs. (2) and (3), respectively. Thus, the potential will be rotated with respect to the film. For $V_0 > 0$ (<0), Eq. (8) describes a triangular (honeycomb) array of adsorption potential maxima and a honeycomb (triangular) array of adsorption potential minima. Various methods, multiple scales analysis, renormalization group theory, and even a "quick and dirty" approach, can be used to derive the free energy in terms of η_{kl} from Eq. (6) assuming that the amplitudes vary on length scales much larger than the atomic spacing. The reader is referred to the multiple references [48–53] for a discussion of such derivations.

However, it is readily apparent that incorporating only the lowest order modes in V and n will only work when the lattice constants of the film and substrate are very similar. When the length of scale of the film and substrate are different the term Vn integrates to zero to lowest order. For example, in the $(\sqrt{3} \times \sqrt{3})$ R30° structure it would be the set of the second largest set of (kl) pairs that coupled to the substrate potential. To illustrate this, it is useful to consider a simple one-dimensional case where the commensurate state is twice the distance between the minima in V, i.e.,

$$n = a_1 \cos(x) + a_2 \cos(2x), \qquad (10)$$

and

$$V = V_0 \cos(2x), \qquad (11)$$

where a_1 and a_2 are the amplitudes of the first two lowest modes in n. Integrating Eq. (6) gives

$$\begin{aligned}
\frac{\mathcal{F}}{2\pi} &= \frac{\Delta B}{4}\left(a_1^2 + a_2^2\right) + \frac{9}{4}B^l a_2^2 - \frac{\tau}{4}a_1^2 a_2 \\
&\quad + \frac{3v}{32}a_1^4\left(a_1^4 + 4a_1^2 a_2^2 + a_2^4\right) + \frac{1}{2}a_2 V_0.
\end{aligned} \qquad (12)$$

As expected the coupling of n to V only occurs through the term $a_2 V_0$, i.e., there is no $a_1 V_0$ coupling. However, minimizing $\mathcal{F}/2\pi$ with respect to a_2, substituting the solution of a_2 that minimizes $\mathcal{F}/2\pi$, and expanding the coupling term in Eq. (12) gives

$$a_2 V_0 = V_0\left(\frac{\tau}{4(9B^l + \Delta B)}a_1^2 + O a_1^4 + \dots\right). \qquad (13)$$

Thus, a_1 is effectively coupled to the potential via the intermediate second mode a_2. A coupling of this sort would also occur if a coupling $\sim Vn^2$ were included in the free-energy functional, since it would produce a term of the form $a_1^2 V_0/4$. Thus, a simpler and more computationally efficient approach would be to use only the smallest modes (smallest $\vec{G}_{kl}$'s, which in this instance would be just a_1) and including the coupling Vn^2 instead using the coupling term Vn, and using the two lowest sets of modes (in this case a_1 and a_2) to describe n.

For higher-order structures (i.e., larger values of j and m), this strategy would require incorporating higher-order coupling terms of the form $n^p V$, where p is some integer. After studying a number of examples and generalizing to arbitrary p, it turns out the minimum value required is $p = (j + 1)m$, whose contribution is

$$F_V = \int d\vec{r} \, n^{(j+1)m} V. \qquad (14)$$

Thus, the appropriate free energy is to replace the nV term in Eq. (6) with $n^{(j+1)m}V$, i.e.,

$$\begin{aligned}
\mathcal{F} = \int d\vec{r}\bigg[&\frac{\Delta B}{2}n^2 + \frac{B^x}{2}n(1 + \nabla^2)^2 n - \frac{\tau}{3}n^3 \\
&+ \frac{v}{4}n^4 + n^{(j+1)m}V\bigg].
\end{aligned} \qquad (15)$$

It should be noted that in this form of the free-energy functional the adsorption potential is an effective one with a different amplitude compared to the true adsorption potential. For the triangular or honeycomb films described by Eq. (7), using the lowest-order modes [i.e., $(kl) = (10),(01)$, and $(\bar{1}\bar{1})$], it can be shown that in the limit where η_{kl} varies on length scales much larger than n, Eq. (15) becomes

$$\begin{aligned}
\mathcal{F}_\eta = \int d\vec{r}\bigg[&\sum_{kl}\left(B^x|\mathcal{G}_{kl}\eta_{kl}|^2 - \frac{3v}{2}|\eta_{kl}|^4\right) \\
&+ \frac{\Delta B}{2}A^2 + \frac{3v}{4}A^4 - 2t\left(\prod_{kl}\eta_{kl} + \text{c.c.}\right) \\
&+ D_{jm}t(\{[(\eta_{10}^*)^j \eta_{01}]^m + \text{c.p.}\} + \text{c.c.})V_0\bigg], \quad (16)
\end{aligned}$$

where $A^2 \equiv 2\sum_{kl}|\eta_{kl}|^2$, $\mathcal{G}_{kl} \equiv \nabla^2 + 2i\alpha\vec{G}_{kl}\cdot\vec{\nabla} + 1 - \alpha^2$, and c.p. stands for cyclic permutations [$(10) \to (01) \to$

$(\bar{1}\bar{1}) \to (10)$ etc.]. The coefficient D_{jm} is a constant given by

$$D_{jm} \equiv \frac{[(j+1)m]!}{(jm)!m!}. \tag{17}$$

A nice feature of this result is that in terms of the amplitudes, only six new terms appear for the coupling independent of (j,m). This free energy functional can now be used to study surface ordering in both the TH and TT systems for all values of j and m.

IV. SMALL DEFORMATION LIMIT AND THE SINE-GORDON MODEL

It is useful to consider the limit of small deformations of Eq. (16) to provide insight into the fundamental dimensionless quantities that control strain induced patterning and to make connection with specific physical systems. In the small deformation limit the amplitudes can be written as

$$\eta_{kl} = \phi e^{i \vec{G}_{kl} \cdot \vec{u}}, \tag{18}$$

where to first order ϕ is a constant and $\vec{u}$ is the displacement vector that enters traditional continuum elasticity theory. The value of ϕ can be estimated by minimizing the free energy with respect to ϕ in the limit that $\vec{u}$ is a constant and V_0 is small. This gives

$$\phi \approx \begin{cases} (t + \sqrt{t^2 - 15v\Delta B})/(15v), & (t>0); \\ (t - \sqrt{t^2 - 15v\Delta B})/(15v), & (t<0), \end{cases} \tag{19}$$

where $t > 0$ ($t < 0$) corresponds to a film of triangular (honeycomb) symmetry. Substitution of Eq. (18) into Eq. (16) gives to lowest order in gradients in $\vec{u}$

$$\mathcal{F}_u \approx \int d\vec{r} \left\{ \frac{C_{11}}{2} [(u_{xx} - \varepsilon)^2 + (u_{yy} - \varepsilon)^2] \right.$$
$$+ 2C_{44}u_{xy}^2 + C_{12}(u_{xx} - \varepsilon)(u_{yy} - \varepsilon)$$
$$\left. + 2V_0 D_{jm}\phi^{(j+1)m} \sum_{kl} \cos \vec{G}_{kl} \cdot \vec{u} \right\}, \tag{20}$$

where C_{ij} are the elastic constants given in Table II and terms independent of $\vec{u}$ have been dropped. Note that in this expansion η_{kl} have been expanded around the lattice constant of the commensurate state, i.e., if $\vec{u}$ is a constant there is an elastic contribution, while if $\vec{u} = \varepsilon \vec{r}$ there is no elastic contribution and $\mathcal{F}_u = 0$. Equation (20) is a 2D sine-Gordon free energy functional. For the boundary conditions relevant for this work there do not exist any analytic solutions for the 2D moiré patterns that minimize $\mathcal{F}_u$ at small V_0. Solutions do, however, exist for one-dimensional striped states as will

TABLE II. The elastic constants for the amplitude model, where ϕ is given in Eq. (19). The elastic parameter $K = (C_{11} + C_{12})^2/C_{11}$ for the TT and TH systems.

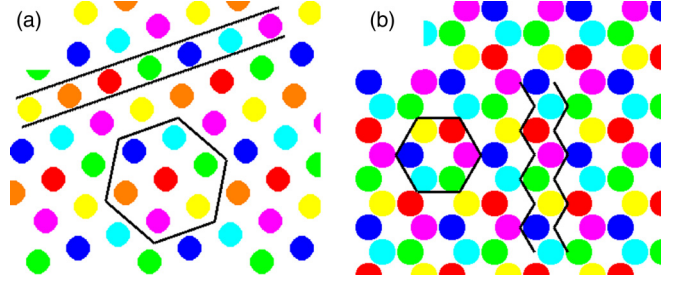| C_{11}	C_{12}	C_{44}	K for TH	K for TT
$9B^x\phi^2$	$3B^x\phi^2$	$3B^x\phi^2$	$16B^x\phi^2$	$144B^x\phi^2/10$

FIG. 7. In (a) the seven commensurate sublattices are shown in different colors for a $(j,m) = (2,1)$ TH system. In (b) the six commensurate sublattices are shown for a $(j,m) = (1,1)$ TT system. In both cases the parallel (or jagged) lines and hexagon encompass the sublattices that correspond to the large-scale stripe and moiré patterns, respectively.

be discussed in the next two subsections for the TH and TT systems.

A. Commensurate to stripe transition in the TH system

Anisotropic one-dimensional solutions or striped states can form along three equivalent directions and one such direction is depicted in Fig. 7(a) for a $(j,m) = (2,1)$ TH system. In such states it is convenient to consider displacements ($\vec{u}$) along the stripe direction and parametrize them in terms of a field Φ as

$$\vec{u} = a_v \frac{\Phi}{2\pi} [\cos(\theta)\hat{x} + \sin(\theta)\hat{y}], \tag{21}$$

where $a_v = 4\pi/\sqrt{3}(a_x^s/L)$ and Φ changes by 2π from one commensurate state to a neighboring one. This gives

$$2V_0 D_{jm}\phi^{(j+1)m} \sum_{kl} \cos \vec{G}_{kl}^v \cdot \vec{u}$$
$$= 2V_0 D_{jm}\phi^{(j+1)m}(2\cos\Phi + 1). \tag{22}$$

To calculate the elastic contribution it is convenient to go into a primed coordinate system $[(x',y') = (x\cos\theta - y\sin\theta, x\sin\theta + y\cos\theta)]$ that is rotated by an angle θ with respect to the horizontal. In these coordinates $\vec{u}$ only depends on x' so the elastic terms become

$$u_{xx} = \cos^2\theta \frac{a_v}{2\pi} \frac{\partial\Phi}{\partial x'}; \quad u_{yy} = \sin^2\theta \frac{a_v}{2\pi} \frac{\partial\Phi}{\partial x'};$$
$$u_{xy} = \frac{a_v}{2\pi} \sin\theta\cos\theta \frac{\partial\Phi}{\partial x'}. \tag{23}$$

Using the fact that for systems of triangular or honeycomb symmetry $C_{11} = C_{12} + C_{44}$, it is straightforward to shown that Eq. (20) reduces to

$$F = A^2 \int dx''dy'' \left[\frac{K}{2} \left(\frac{\partial\Phi}{\partial x''} - \varepsilon \right)^2 + W\cos\Phi \right], \tag{24}$$

where a constant term has been neglected, and $x'' = x'/A$, $y'' = y'/A$, $A \equiv a_v(C_{11} + C_{12})/(2\pi C_{11})$,

$$W = 4V_0 D_{jm}\phi^{(j+1)m}, \tag{25}$$

and

$$K = \frac{(C_{11} + C_{12})^2}{C_{11}}. \tag{26}$$

Equation (24) is a 1D sine-Gordon model that in the mean-field limit has an incommensurate-commensurate phase transition at a critical value of $(W/K)_c$ [58] given by

$$\left[\frac{W}{K}\right]_c = \frac{\pi^2}{16}\varepsilon^2 = \frac{4D_{jm}\phi^{(j+1)m}C_{11}}{(C_{11}+C_{12})^2}V_0, \qquad (27)$$

such that for $W/K < (W/K)_c$ $[W/K > (W/K)_c]$ the incommensurate striped (commensurate) state has the lowest energy. As the transition is approach from below $(W/K)_c$, the wavelength of the striped state diverges which can be expected because a commensurate state can be thought of as a striped state with an infinite wavelength. Although thermal fluctuations are not considered in the present work, it is possible that they will change the nature of this phase transition.

B. Commensurate to stripe transition in the TT system

The striped state for the TT system is depicted in Fig. 7(b). The displacement vector from one stripe to the next can be written as

$$\vec{u} = \vec{\delta} + \frac{\Phi(r)}{2\pi}\vec{\delta}, \qquad (28)$$

where

$$\frac{\vec{\delta}}{a_x^s} = \frac{1}{2}\left[\left(\cos\theta - \frac{\sin\theta}{\sqrt{3}}\right)\hat{x} + \left(\sin\theta + \frac{\cos\theta}{\sqrt{3}}\right)\hat{y}\right]. \quad (29)$$

It is straightforward to show that for this displacement

$$2V_0 D_{jm}\phi^{(k+1)m}\sum_{kl}\cos\left(\vec{G}_{kl}^v \cdot \vec{u}\right)$$

$$= 2V_0 D_{jm}\phi^{(j+1)m}\left[\cos\left(\frac{2\Phi + 4\pi}{3}\right)\right.$$

$$\left. + 2\cos\left(\frac{\Phi + 2\pi}{3}\right)\right], \qquad (30)$$

for all k. To a good approximation this form can be fitted to $\cos\Phi$ as

$$2V_0 D_{jm}\phi^{(k+1)m}\sum_{kl}\cos\left(\vec{G}_{kl}^v \cdot \vec{u}\right)$$

$$\approx -\frac{2V_0 D_{jm}\phi^{(j+1)m}}{4}(5 + \cos\Phi). \qquad (31)$$

A comparison of this approximation and the exact solution is shown in Fig. 8. Similar to the TH case the elastic terms can be be simplified so that the 2D sine-Gordon model can be transformed into a 1D model, i.e., Eq. (24) with

$$W = \frac{1}{2}D_{jm}\phi^{(j+1)m}V_0; \quad K = \frac{(C_{11}+C_{12})^2}{C_{11}+C_{44}/3}. \quad (32)$$

Again, the stripe-commensurate transition occurs at the critical value of W/K,

$$\left[\frac{W}{K}\right]_c = \frac{\pi^2}{16}\varepsilon^2 = \frac{D_{jm}\phi^{(j+1)m}(C_{11}+C_{44}/3)}{2(C_{11}+C_{12})^2}V_0. \quad (33)$$

To summarize the results in this section, in Table III some tabulated critical values for the 1D sine-Gordon model for the TH and TT are given. The dimensionless ratio W/K is
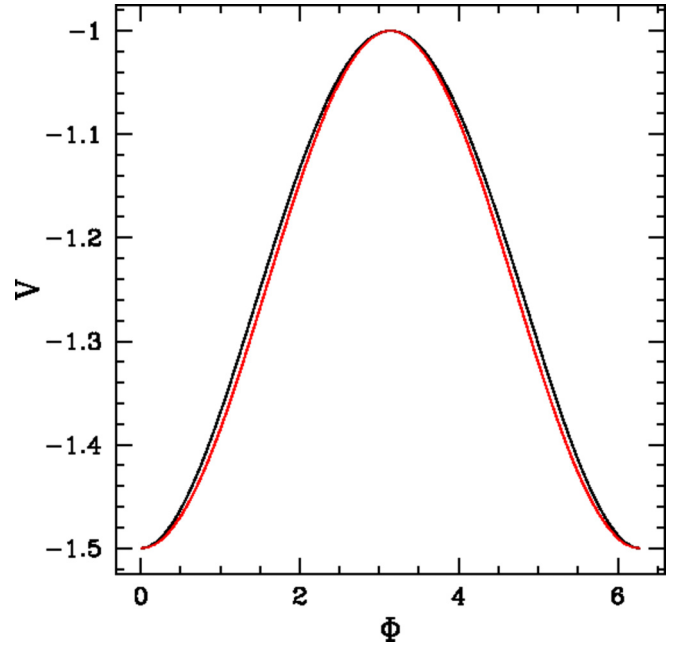

FIG. 8. The figure shows the exact potential Eq. (30) (black line) compared to the approximate solution given in Eq. (31) (red line).

essentially the ratio of adhesion energy to elastic energy. When it is large the commensurate states dominate and when it is small incommensurate states (not necessarily striped states) emerge as will be shown in the next sections. This ratio can be used to make connection with physical realizations of the TH and TT adsorbate systems as it can be calculated using quantum density functional theory or classical interatomic potentials assuming accurate potentials are available. The ratio W/K can be calculated within a single unit cell of the commensurate state by calculating four energies per unit area, namely the energy density of a perfectly commensurate state E^{tot}, that of a perfectly incommensurate state at zero strain E^{min}, that of a perfectly incommensurate state at the given misfit strain E^{sl}, and the surface energy of the substrate E^{sub}. The strain energy density is then given by $E^s = E^{\text{sl}} - E^{\text{min}}$ and the commensurate energy density is $E^c = E^{\text{tot}} - E^{\text{sub}} - E^{\text{min}}$. The adhesion can then be defined as

$$W = E^s - E^c. \qquad (34)$$

The value of K can be determined by measurements of the elastic moduli. Estimates of W/K for various systems have been given in Refs. [25,46].

TABLE III. Critical values of the effective coupling coefficient in the sine-Gordon model.

State characterization				$(W/K)_c/\varepsilon^2$	
System	j	m	D_{jm}	TH	TT
(1×1)	0	1	1	$V_0/(4B^x\phi)$	$10V_0/(72B^x\phi)$
(2×2)	0	2	1	$V_0/(4B^x)$	$10V_0/(72B^x)$
$(\sqrt{3}\times\sqrt{3})\text{R}30°$	1	1	2	$V_0/(2B^x)$	$10V_0/(144B^x)$
$(\sqrt{7}\times\sqrt{7})\text{R}19.1°$	2	1	3	$3V_0\phi/(4B_o^x)$	$10V_0\phi/(24B^x)$

V. EQUILIBRIUM STATES AND PHASE DIAGRAMS

Phase diagrams were numerically determined as a function of mismatch strain (ε) and adsorption strength (using the dimensionless variable W/K) for some specific systems. The diagrams were obtained by minimizing the free-energy functional given in Eq. (16) for various patterns using a simple relaxational (nonconserved) algorithm, i.e.,

$$\frac{\partial \eta_{kl}}{\partial t} = -\frac{\delta \mathcal{F}_\eta}{\delta \eta_{kl}^*}. \qquad (35)$$

In the case of the TH system, the patterns compared were stripes and a 2D array of triangular commensurate regions. For the TT systems stripes and a 2D array of honeycomb commensurate regions were examined. In the latter case it was found that there was a small region in phase space (between the honeycomb and stripe regions) in which junctions in the 2D patterns break into dislocation pairs for the (1×1) system or twist for all the higher order systems. While it is possible that there exist other patterns that minimize the free-energy functional, numerical simulations from random initial conditions indicate that these are the lowest-energy patterns. In the next subsection results are given for the TH system, followed by an examination of the TT system in Sec. V B.

A. Triangular on honeycomb (TH) systems

The (1×1) and $(\sqrt{3} \times \sqrt{3})\,R30°$ systems have been studied in prior publications [11,46,47]. In these cases the phase diagram is dominated by 2D moiré patterns for $(W/K) < (W/K)_c$ that consist of a honeycomb network of domain walls and a triangular pattern of commensurate regions. The region defined by $W/K > (W/K)_c$ is dominated by the commensurate phase. A small sliver of a striped state may exists in between the low and high W/K regions. In all the cases examined here, except for the (1×1) structure [i.e., $(\sqrt{3} \times \sqrt{3})\,R30°$, (2×2), and $(\sqrt{7} \times \sqrt{7})\,R19.1°$] a stripe region always separates the 2D moiré patterns from the commensurate state. For the (1×1) system the striped state does not exist for small strains but there exists a triple point when the stripe region appears corresponding to the coexistence of striped, 2D moiré, and commensurate phases. Below a number of specific systems are discussed in detail.

1. $(\sqrt{3} \times \sqrt{3})\,R30°$, $(j,m) = (1,1)$

In Sec. III it was argued that the lowest-order coupling was given by Eq. (14), or for $(j,m) = (1,1)$, a term of the form $\int d\vec{r}\, n^2 V$. It is reasonable to question whether or not the full PFC model or a different nonzero coupling would lead to different results. For this reason numerical investigations were also conducted using the full PFC model, and the APFC model with a $n^3 V$ coupling in addition to the $n^2 V$ coupling mentioned above. For comparison the results are presented on the W/K versus $\varepsilon|\varepsilon|$ plane (recalling that the sine-Gordon prediction for the stripe-commensurate transition occurs when $W/K = \pi^2/16\varepsilon|\varepsilon|$). The relationship between W/K and the model parameters was discussed in Sec. III for the lowest-order coupling (i.e., $n^2 V$ in this instance). The $n^3 V$ coupling makes the following contribution to the free energy:

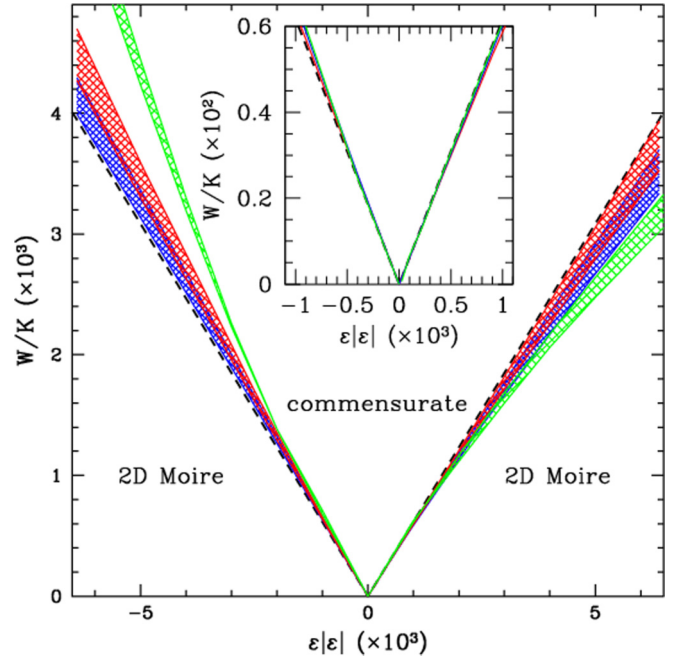$$F_V = 3V_0\big(\eta_1^2\eta_2 + \eta_1\eta_2^2 + \text{c.p.} + \text{c.c.}\big), \qquad (36)$$

FIG. 9. Phase diagram for TH $(\sqrt{3} \times \sqrt{3})\,R30°$ ordering using the full PFC model with nV coupling (green), the APFC model with $n^2 V$ (red) and $n^3 V$ (blue) coupling. The black dashed lines correspond to the sine-Gordon solution for the stripe-commensurate transition. In each case in the hatched region the stripe state is the lowest energy state and below (above) this region the 2DM (commensurate) state is the lowest energy state. The $n^2 V$ result is redrawn from Ref. [47].

which contributes $24 V_0 \phi^3 \cos \Phi$ to the sine-Gordon equation, i.e.,

$$W = 24 V_0 \phi^3. \qquad (37)$$

This coupling does not change the value of K so it is then straightforward to calculate W/K for the $n^3 V$ coupling. For the full PFC model it is difficult to analytically derive an expression for the values of W since it involves nonlinear coupling of several modes. However, for small values of ε the continuum sine-Gordon result for the stripe-commensurate transition should be valid. At small ε the slope of V_0 versus $\varepsilon|\varepsilon|$ was measured for both negative and positive values of ε. For comparison with the APFC results V_0 was multiplied by $\pi^2/16$ and divided by the slope measured.

Figure 9 displays the phase diagram for all three models and very similar results are obtained. In these phase diagrams three specific phases are observed, namely the 2D moiré, striped, and commensurate states. Examples of the 2D moiré and striped patterns are shown in Fig. 10. These figures were obtained by first reconstructing the dimensionless density difference n using Eq. (7) and then finding all the maxima in n. In Fig. 10 (and in all the sample patterns to follow) the positions of these maxima are plotted as points whose color is determined from the distance of the point from the various sublattices. More specifically, the color is an average of the colors shown in Fig. 6(a) with a weighting inversely proportional to the distance to the closest neighbor of the corresponding sublattice.
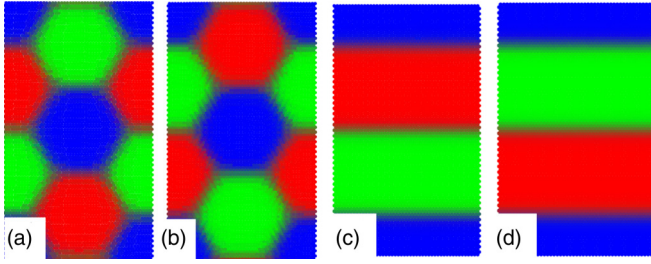
FIG. 10. Sample 2D moiré (a and b), and stripe (c and d), patterns for $\varepsilon = -3$ % (a and c) and $\varepsilon = +3$ % (b and d), obtained from the n^3V coupling in the TH $(\sqrt{3} \times \sqrt{3})$ R30° system. In (a) $(W/K, L_x, L_y) = (-0.05432 \times 10^{-2}, 364.0, 630.5)$, (b) $(W/K, L_x, L_y) = (-0.05160 \times 10^{-2}, 380.0, 658.2)$, (c) $(W/K, L_y) = (-0.05786 \times 10^{-2}, 584.0)$, and (d) $(W/K, L_y) = (-0.05378 \times 10^{-2}, 588.0)$.

It is interesting to note that the triangular pattern exactly matches the sublattice pattern on a larger scale which can be see by comparing Figs. 10(a) and 10(b) with Fig. 6(a). Moving across a stripe or through a hexagonal region in the 2D patterns, the change in color depends on the sign of ε. For example, for $\varepsilon = -3\%$, the colors change from red to blue to green (also note that the systems are periodic) as seen in Figs. 10(a) and 10(c). In contrast for $\varepsilon = +3\%$, the colors change from red to green to blue as seen in Figs. 10(b) and 10(d). When the commensurate state corresponds to a tensile (compressive) strain on the film, domain walls appear when the atoms slip
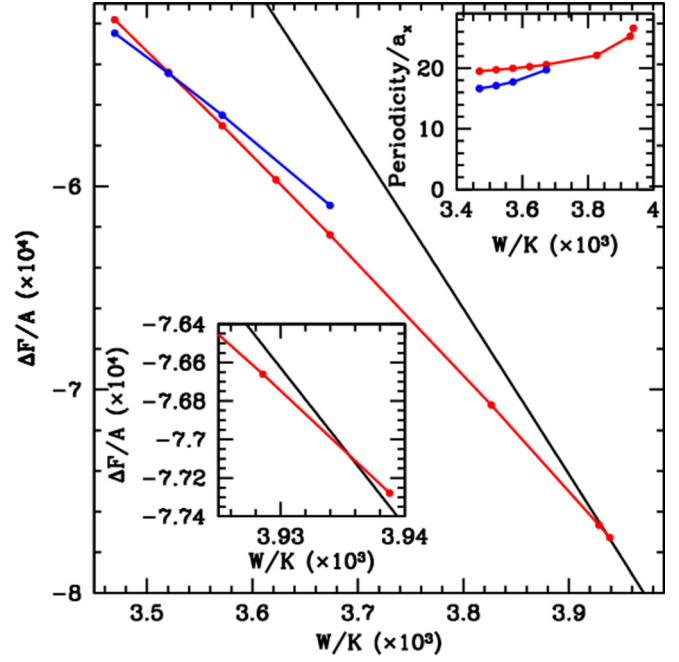

FIG. 12. Free-energy density difference from an incommensurate ($W/K = 0$) state as a function of W/K for 2D moiré (blue), striped (red), and commensurate (black) phases at $\varepsilon = 8\%$. In the bottom left inset is a blowup showing that the free energy of the stripes becomes higher than that of the commensurate phase indicating a discontinuous phase transition. In the top inset the periodicity of the 2D moiré (blue) and striped (red) states is shown.
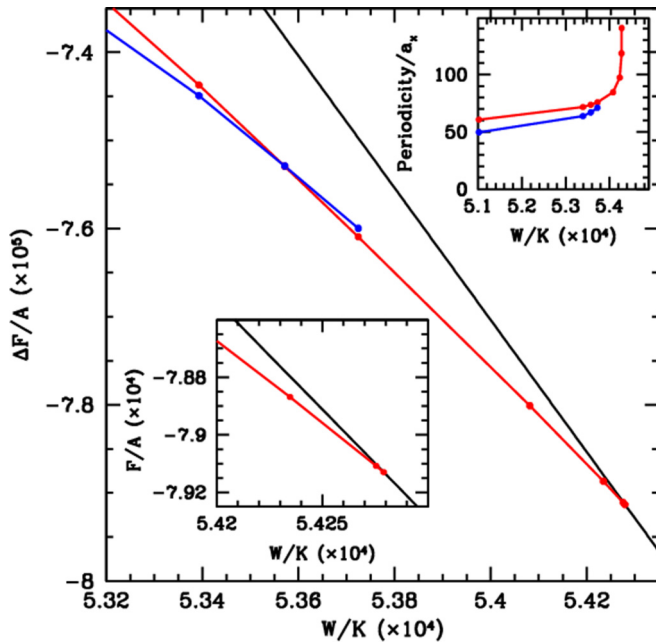
to the closest degenerate commensurate state that is a further (nearer) away.

The transition from the 2D moiré to a striped incommensurate phase is a discontinuous transition as it is not possible for the 2D pattern to continuously deform into a stripe. This is illustrated in Figs. 11 and 12 for $\varepsilon = 3\%$ and 8%, respectively, for the n^2V coupling (similar behavior is observed for the full PFC model and the n^3V coupling). In these figures it is clear that the lowest free energy density changes discontinuously as a function of W/K when the lowest energy states changes from 2D moiré to striped states. For small values of ε the transition from striped to commensurate states appears to be continuous (in the absence of thermal fluctuations) as predicted by the 1D sine-Gordon model. This can be seen in the bottom left inset in Fig. 11 as the slope free energy density of the stripe state approaches that of the commensurate state at the transition, and as shown in the top right inset in the figure the stripe wavelength diverges. A continuous transition is possible as a stripe can continuously change into a commensurate state, i.e., the commensurate state is a stripe of infinite wavelength. This behavior is in contrast to the large ε behavior where the stripe - commensurate transition becomes discontinuous. This is illustrated in the bottom left inset in Fig. 12 as there exists above the transition a metastable stripe phase that has a higher energy than the commensurate phase. In addition the figure also shows that the stripe periodicity does not diverge at the transition. It is likely that the discrete nature of the system starts to play a larger role at larger strains causing this effect.
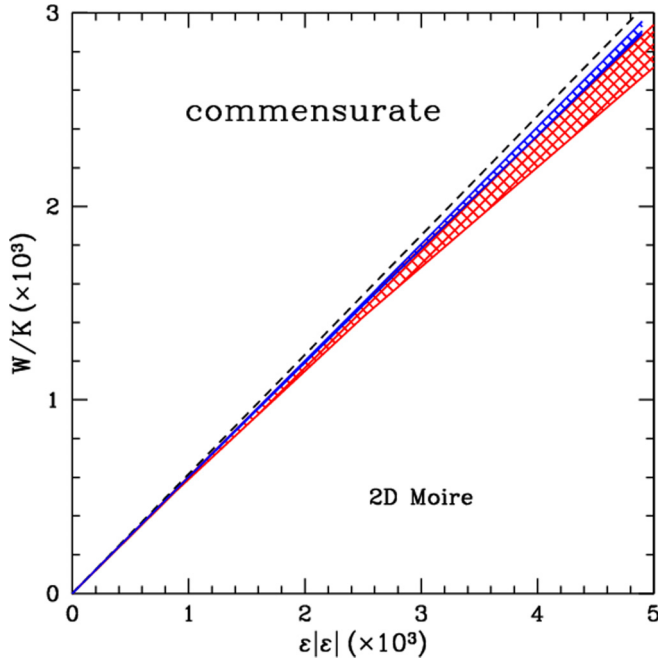

FIG. 11. Free-energy density difference from an incommensurate ($W/K = 0$) state as a function of W/K for 2D moiré (blue), stripe (red), and commensurate (black) phases at $\varepsilon = 3\%$. In the bottom left inset is a blowup showing that the free energy of the striped phase never becomes higher than that of the commensurate phase indicating a continuous phase transition. In the top inset the periodicity of the 2D moiré (blue) and striped (red) states is shown.

FIG. 13. Phase diagram for the (2×2) and $(\sqrt{7} \times \sqrt{7}) \text{R}19.1°$ systems in blue and red, respectively. The hatched regions correspond to parameter ranges where the stripe phase is the ground state.

2. Higher-order systems (2×2), $(j,m) = (0,2)$ and $(\sqrt{7} \times \sqrt{7}) \text{R}19.1°$, $(j,m) = (2,1)$.

The (2×2) and $(\sqrt{7} \times \sqrt{7}) \text{R}19.1°$ orderings have four and seven commensurate sublattices, respectively. Despite this complication the phase diagrams look very similar to the $(\sqrt{3} \times \sqrt{3}) \text{R}30°$ one as shown in Fig. 13. The (2×2) system has a smaller stripe region than the $(\sqrt{7} \times \sqrt{7}) \text{R}19.1°$ but in both cases the stripe region appears to exist for all values of ε. Sample configurations for the 2D moiré and 1D stripe patterns are shown for both systems in Fig. 14. As with the $(\sqrt{3} \times \sqrt{3}) \text{R}30°$ both the 1D and 2D patterns are determined by the ordering of the degenerate sublattice states.
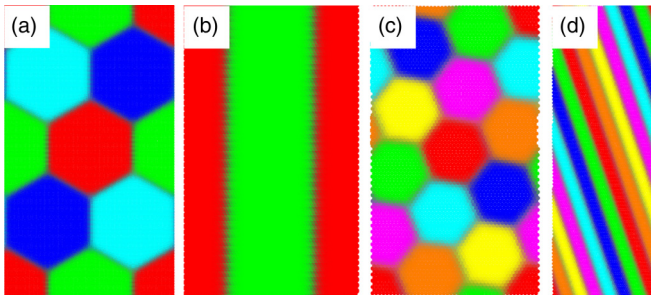

FIG. 14. Sample 2D moiré and striped ordering patterns in (a) and (b), respectively, for the TH (2×2) system with a misfit strain of $\varepsilon = 2\%$ at $W/K = 0.242 \times 10^{-3}$ and 0.244×10^{-3}, respectively. The widths of the systems in (a) and (b) are $382 \, a_x$ and $56 \, a_x$, respectively. 2D moiré and striped patterns in (c) and (d), respectively, for the TH $(\sqrt{7} \times \sqrt{7}) \text{R}19.1°$ system with $W/K = 1.358 \times 10^{-3}$ and $\varepsilon = 5\%$. Figure (a) has a lower free energy per unit area than (b). The widths of the systems here are $49 \, a_x$ and $53 \, a_x$ in (c) and (d), respectively.
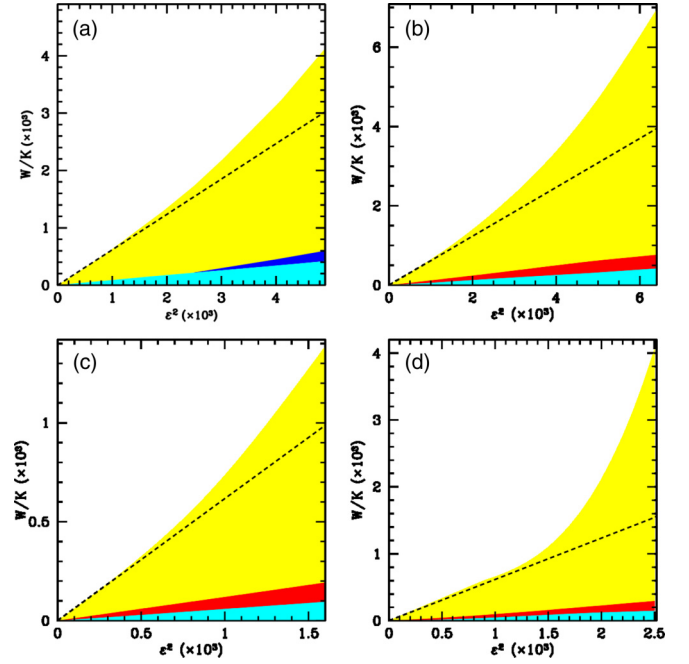

FIG. 15. Phase diagrams for various TT systems. The white, yellow, red, cyan, and blue regions correspond to the commensurate, striped, twisted 2D moiré, 2D moiré, and zigzag phases, respectively. The dashed line corresponds to the sine-Gordon prediction for the stripe-commensurate transition. See text for details. (a) 1×1; (b) $\sqrt{3} \times \sqrt{3} \text{R}30°$; (c) 2×2; and (d) $\sqrt{7} \times \sqrt{7} \text{R}19.1°$.

In addition the nature of the phase transitions are identical to the $(\sqrt{3} \times \sqrt{3}) \text{R}30°$ system, i.e., the 2D moiré to stripe transition is discontinuous and the stripe to commensurate transition is continuous at small ε and discontinuous at large ε.

B. Triangular on triangular (TT) systems

The phase diagram for a film of triangular symmetry adsorbed on a substrate that has a triangular pattern of maxima (or honeycomb pattern of minima) gives rise to much richer features than the TH system. The case of a (1×1) or $(j,m) = (0,1)$ system was explored in prior
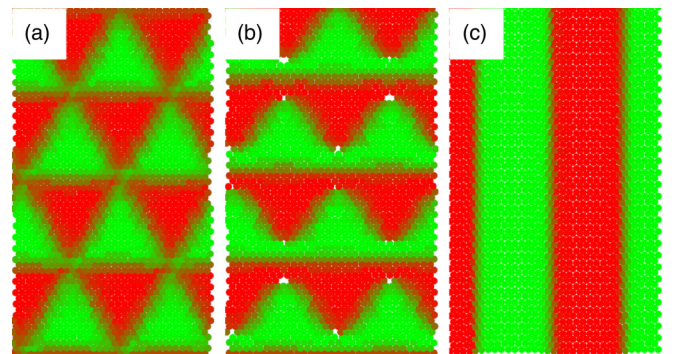

FIG. 16. Sample configurations for the TT (1×1) system showing 2D moiré, zigzag and striped phases in (a), (b), and (c), respectively at $\varepsilon = 7\%$. Here $W/K = 0.399 \times 10^{-3}$, 0.599×10^{-3}, and 4.051×10^{-3} in (a), (b), and (c), respectively.
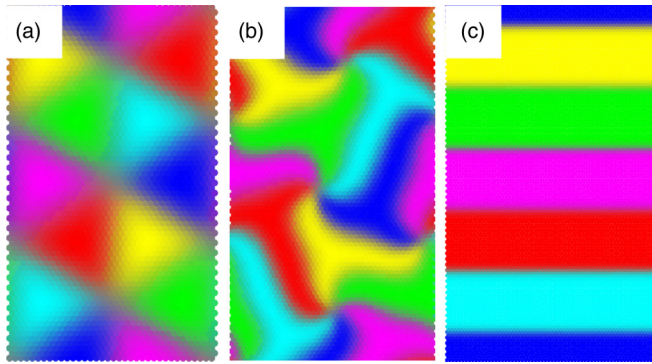
FIG. 17. Sample configurations for the TT $(\sqrt{3} \times \sqrt{3})\,\mathrm{R}30°$ system showing 2D moiré, twisted 2D moiré, and striped states in (a), (b), and (c), respectively, at $\varepsilon = 3\%$. Here $W/K = 0.574 \times 10^{-3}$, 0.112×10^{-3}, and 0.574×10^{-3} in (a), (b), and (c), respectively.

FIG. 19. Sample configurations for the TT $(\sqrt{7} \times \sqrt{7})\,\mathrm{R}19.1°$ case with 2D moiré, twisted 2D moiré, and striped states in (a), (b), and (c), respectively, at $\varepsilon = 3\%$. Here $W/K = 0.0377 \times 10^{-3}$, 0.0566×10^{-3}, and 0.377×10^{-3} in (a), (b), and (c), respectively.

publications [24,25], but has not been examined for higher-order systems. Detailed phase diagrams were calculated for the $(\sqrt{3} \times \sqrt{3})\,\mathrm{R}30°$ $[(j,m) = (1,1)]$, $(2 \times 2)[(j,m) = (0,2)]$, and $(\sqrt{7} \times \sqrt{7})\,\mathrm{R}19.1°[(j,m) = (2,1)]$ systems and compared with the (1×1) case. The phase diagrams for all these systems are shown in Fig. 15. The typical 1D and 2D patterns that emerge in these systems are shown in Figs. 16, 17, 18, and 19 for the (1×1), $(\sqrt{3} \times \sqrt{3})\,\mathrm{R}30°$, (2×2), and $(\sqrt{7} \times \sqrt{7})\,\mathrm{R}19.1°$ systems, respectively.

In all cases as W/K is decreased there exists a transition from a commensurate to a striped incommensurate state that for small ε is well predicted by the sine-Gordon prediction given in Eq. (33). In all cases except for the (1×1), this is followed by a transition from the incommensurate striped state to an incommensurate 2D twisted moiré pattern, which is illustrated in Figs. 17(b), 18(b), and 19(b) for the $(\sqrt{3} \times \sqrt{3})\,\mathrm{R}30°$, (2×2), and $(\sqrt{7} \times \sqrt{7})\,\mathrm{R}19.1°$ orderings, respectively. As W/K is lowered further this is followed by a transition from the incommensurate 2D twisted moiré pattern

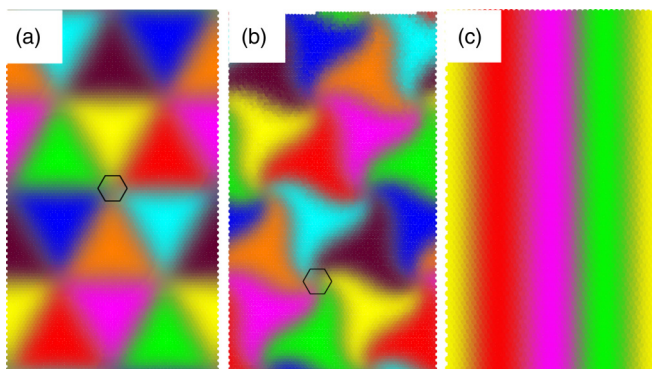to an untwisted 2D moiré pattern. This latter transition is continuous as the twisted pattern continuously untwists as the transition is approached from above as shown in Fig. 20. This is also shown in Fig. 21(a), which displays the free-energy density difference per area A ($\Delta F/A$) of the twisted and untwisted states as a function of W/K. As can been seen in this figure, $\Delta F/A$ for the twisted state continuously approaches the slope of $\Delta F/A$ for the untwisted state. The transition from the twisted 2D moiré state to the stripe phase is discontinuous as there is no continuous deformation from a twisted 2D pattern to a stripe. This is also verified in Fig. 21(b) which shows $\Delta F/A$ of the 2D twisted state to cross $\Delta F/A$ for the striped state as the transition is approached from small to large W/K.

Similar to the TH systems the stripe-to-commensurate transition was observed to be continuous for small ε and discontinuous for large ε for the $(\sqrt{3} \times \sqrt{3})\,\mathrm{R}30°$ system. In this instance the discontinuity in the free energy is very small and challenging to detect when plotting $\Delta F/A$ versus W/K for the two phases. It is, however, easier to see when plotting $\Delta F/A$ versus a_x/λ, where λ is the periodicity of the striped state and $a_x/\lambda = 0$ corresponds to the commensurate state. As shown in Fig. 21(c), $\Delta F/A$ has only one minima that approaches zero as the transition is approached at at $\varepsilon = 3\%$ indicating a continuous transition. This is in contrast

FIG. 18. Sample configurations for the TT (2×2) case showing 2D moiré, twisted 2D moiré, and striped states in (a), (b), and (c), respectively, at $W/K = 0.039 \times 10^{-3}$ and $\varepsilon = 2\%$. Figure (b) has a lower free energy per unit area than (a) or (c). The widths of the figures are $440a_x$, $448a_x$, and $288a_x$ in (a), (b), and (c), respectively. The black hexagons at the junctions in a) and b) contain 61 density maxima in n. The average distance where these maxima lie from the potential maxima is $0.67a_x$ and $0.80a_x$ implying that the twisted junctions have a lower potential energy.
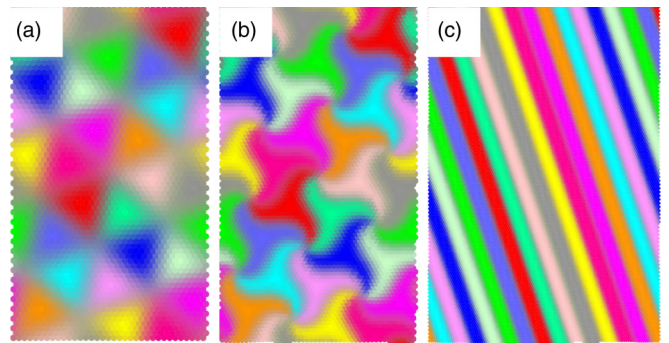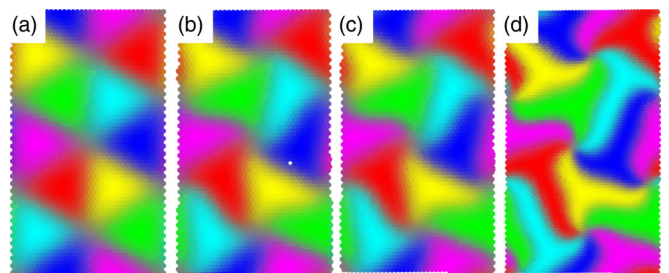

FIG. 20. Series of configurations for the TT $(\sqrt{7} \times \sqrt{7})\,\mathrm{R}19.1°$ system showing colored density maxima plots of the 2D twisted moiré state. In panel (a) the honeycomb state is at $(V_0, \varepsilon, Lx) = (0.00076, 3\%, 130)$, and the twisted honeycomb states in (b)–(d) correspond to $(V_0, \varepsilon, L_x) = (0.00078, 3\%, 132)$, $(0.00081, 3\%, 138)$, and $(0.00150, 3\%, 170)$.
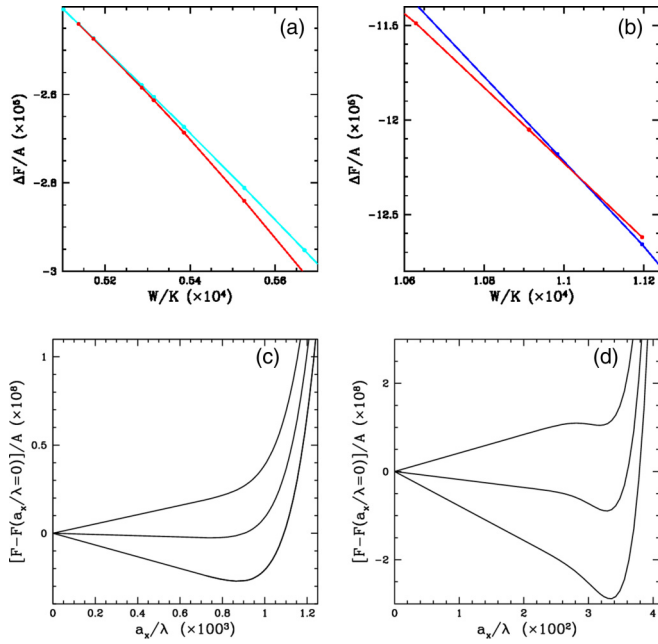
FIG. 21. The free-energy density difference from the incommensurate ($W/K = 0$) state is shown as a function of W/K for twisted and untwisted 2D moiré patterns in red and cyan, respectively, in panel (a), and for twisted 2D moiré and striped states in red and blue, respectively, in panel (b). In panels (c) and (d) the free-energy density difference from the commensurate state is show as a function of inverse stripe wavelength (λ) at $\varepsilon = 3\%$ and 8%, respectively. In panel (c) the lines from bottom to top correspond to $W/K = 5.7115 \times 10^{-4}, 5.7132 \times 10^{-4}$, and 5.7150×10^{-4}, respectively. In panel (d) the lines from bottom to top correspond to $1.89413 \times 10^{-2}, 1.89449 \times 10^{-2}$, and 1.89484×10^{-2}, respectively.
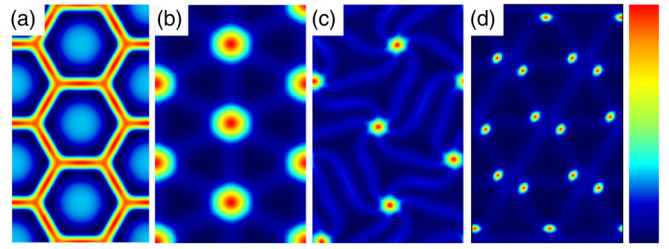

FIG. 22. Spatial plot of the local free energy densities for (a) TH $(\sqrt{3} \times \sqrt{3})$ R30° system at $(\varepsilon, W/K) = (3\%, 0.5357 \times 10^{-3})$; (b) and (c), TT $(\sqrt{3} \times \sqrt{3})$ R30° system at $(\varepsilon, W/K) = (3\%, 0.0574 \times 10^{-3})$ and $(\varepsilon, W/K) = (3\%, 0.1063 \times 10^{-3})$, respectively; and (d) a (1×1) system at $(\varepsilon, W/K) = (7\%, 1.997 \times 10^{-3})$. The energy scale from low (blue) to high (red) is shown on the right in arbitrary units.

to $\varepsilon = 10\%$ where, as seen in Fig. 21(d), where there exists two minima in $\Delta F/A$, one at $a_x/\lambda = 0$ and the other at a finite value of a_x/λ. As the transition is approached from below, the minimum that is lowest changes discontinuously indicating a discontinuous phase transition. In the (2×2) and $(\sqrt{7} \times \sqrt{7})$ R19.1° systems it was difficult to obtain reliable results for large ε indicating the model may not be applicable in this limit for these systems and hence the change from a continuous to a discontinuous transition could not be verified.

It should be noted that the results differ for the (1×1) case where for small ε there is a transition from the striped state into an untwisted 2D moiré pattern, while at large ε there exists a zigzag state [illustrated in Fig. 15(b)], which contains a periodic array of dislocations. The transition from the 2D moiré patterns to the zigzag state is discontinuous.

C. Energy considerations

The phase diagrams of the TH and TT systems are remarkably different, the latter being much more complex and containing an extra phase (zigzag or twisted 2D moiré states). The reason for this was discussed in a previous publication [11] that examined the (1×1) system. The difference can be ascribed to the large difference in junction versus domain wall energies. If the junction energy is much larger than the domain wall energy one would expect that the transition to

the striped states would occur at a much lower value of W/K. The spatial free energy density plots for the 2D moiré patterns in the TH and TT $(\sqrt{3} \times \sqrt{3})$ R30° cases are compared in Figs. 22(a) and 22(b) just below the transition to this state [from either striped (TH) or twisted 2D (TT) states]. In the TH case the domain walls and junctions (in red) form a honeycomb network, while the commensurate regions (in blue or light blue) form a triangular pattern. In contrast, in the TT case the domain walls (in light blue) and junctions (in red) for a triangular network and the commensurate regions (in dark blue) form a honeycomb pattern. These figures clearly show that the relative junction to domain wall energy is much larger in the TT case. In the TH case the junction and domain wall energies are comparable and in some cases the junction energies can be lower than the domain wall energies. Similar comparison also applies to the (1×1)[11], (2×2), and $(\sqrt{7} \times \sqrt{7})$ R19.1° systems. As explained in Ref. [11] the difference arises as the change in the displacement vector $\vec{u}$ is larger going through a junction than a domain wall in the TT case.

The very large relative junction energy in the TT case is the reason why the stripe phase appears at much lower values of W/K than the TH case. It is also the reason why the new 2D twisted moiré and zigzag patterns appear in the TT phase diagrams, whose free energy landscapes are shown in Figs. 22(c) and 22(d), respectively. In the $(\sqrt{3} \times \sqrt{3})$ R30°, (2×2), and $(\sqrt{7} \times \sqrt{7})$ R19.1° systems the twisted state increases the total length of the domain walls, which implies that the "twist" must lead to a lowering of the junction energies. A close examination of the maxima of the density near the junction reveals that these maxima are further from the maxima of the potential energy $V(\vec{r})$ in the twist case. More specifically, in the (2×2) TT case the average distance where the 61 maxima closest to the junction (see Fig. 18) are from the maxima in $V(\vec{r})$, is $0.67a_x$ for the twisted case as compared to $0.80a_x$ for the untwisted case. Thus, the system twists to lower the potential energy of the junctions even though this increases the length of the domain walls connecting the junctions.

In the (1×1) case the change in the magnitude of the displacement vector across both domain walls and the junction is larger than in the other systems since the degenerate sublattices are further apart relative to the preferred lattice

constant of the film (typically the relative distance decreases as j and m are increased). In the TT (1×1) case the junction energy becomes so large that it splits into two dislocation pairs. The creation of the pairs will probably depend on the energy of the dislocation cores.

The (1×1)TH system also differs from the other TH systems in that for small ε there exists a direct transition from the 2D moiré patterns with no stripe state in between (to the accuracy of the numerical calculations). The stripe states only appear for large values of ε[11]. This is somewhat similar to the (1×1)TT case in which the zigzag state only appears at large values of ε. This effect must be due to a subtle interplay between the junction and domain wall energies. In the (1×1)TH case it was found that for small (large) ε the junction energy was slightly lower (higher) than the domain wall energy which may explain this phenomenom. However, as shown in Ref. [47] this also occurs in the TH $(\sqrt{3} \times \sqrt{3})$ R30° system and a stripe region in the phase diagram exists for all values of ε within our numerical accuracy.

VI. COMPARISON WITH EXPERIMENTS

An important initial motivation for this work was to understand the patterns that form in the Cu/Ru(0001) system, which is a TT (1×1) system in the notation used in this work. Experiments in that system reveal that the patterns that the film form depend strongly on the number of monolayers that are adsorbed, such that one monolayer is commensurate, two monolayers are in a zigzag state, three monolayers are in a striped state, and finally four layers are in a honeycomb state. While the simplistic approach used in this work only considers 2D monolayers it can be argued—and has been verified in density functional calculations on the Cu/Pd(111) system—that the effective W/K decreases with increasing number of layers as the effective adhesion energy decreases with increasing layer thickness, and the total strain energy per unit area increases in the commensurate state.

To compare with experiments, simulations were done on micron sized systems where W/K was decreased from a value in the commensurate region to a value in the striped, zigzag or 2D moiré regions and then held fixed to observe subsequent ordering. These simulations were meant to mimic the experimental procedure of adding layers (lowering W/K) and then annealing the system for some time at a given coverage. As shown in our earlier works [24,25], the results are remarkably consistent with experimental results of Gunther *et al.* [23] in both the nature of the patterns and the selected length scales. In the present work additional simulations were conducted to examine the dynamics of ordering in the large W/K commensurate region or the monolayer or submonolayer limit. The patterns that emerge in this limit were also consistent with experiments performed by Schmid *et al.* [27] as shown in Fig. 23.

The HT (1×1) system is relevant for graphene ordering on a wide range of metallic substrates and has been analyzed in some detail in Refs. [11,46]. In the latter work quantum mechanical density functional theory calculations (DFT) were used to parametrize specific systems, i.e., to calculate W/K for a given graphene-substrate system. For most of the graphene on (111) substrates (Pd, Pt, Al, Ag, and Au), the value of W/K is well below the transition to striped or commensurate
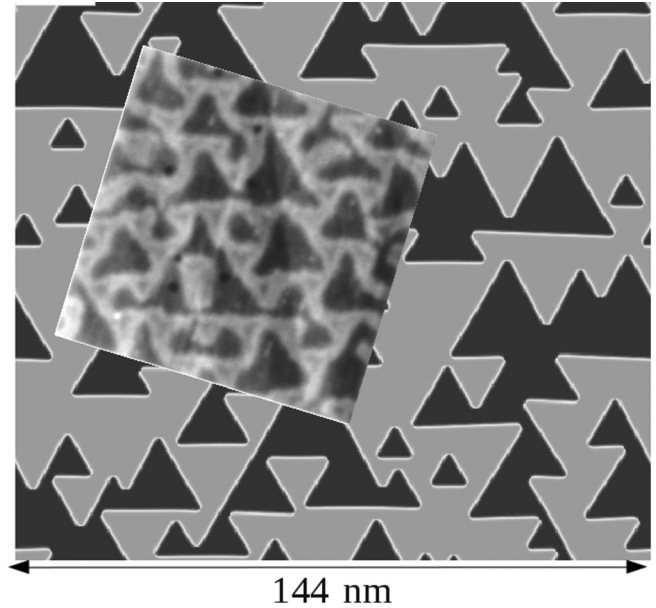

144 nm

FIG. 23. Comparison between numerically simulated ordering in the large W/K limit for the (1×1)TT system with experimental results of Schmid *et al.* [27] on the ordering of a partially filled monolayer in the Cu/Ru(0001) system. The experimentally observed pattern is shown as an overlay on a typical configuration (number density plot) from the simulations.

states, implying that 2D moiré patterns should be observed experimentally, which is also the case. The value of W/K calculated for graphene on Cu(111) is just below the transition line also implying 2D moiré patterns. Finally, the value for graphene on Ni(111) is well above the transition line (i.e., in the commensurate region) implying that no moiré patterns should occur, which is consistent with experiments [59,60].

The influence of the film-substrate misorientation was also examined [46]. It was found that the periodicity λ of the 2D moiré patterns decreases with the misorientation angle θ_m although surprisingly the state with the lowest energy was not at $\theta_m = 0$. It was found to be at $\theta_m = 0.88°$ for Cu(111) and 3.22° for Pt(111). The behavior of the λ as a function of θ_m was found to be consistent with experiments although the experimental data of Merino *et al.* [3] is somewhat inconclusive.

The $(\sqrt{3} \times \sqrt{3})$ R30° TH class of systems includes Xe on graphite [40], Kr on graphite [41], and Xe/Pt(111)[42]. As discussed in Ref. [47], the appearance of striped and 2D moiré patterns is consistent with experimental observations in the Xe/Pt(111) system while only the latter pattern has been seen in Kr on graphite and Xe on graphite.

One of the unexpected predictions of this work is the appearance of the twisted 2D pattern that emerges in TT (or HH) systems. Even though the region of the phase diagram where such pattern would be observed is relatively small there is experimental and theoretical evidence of these patterns in a number of systems as illustrated in Fig. 24. They include experiments of TiO_x ordering on Au(111) surfaces [61,62], simulations of Au on Ru(0001)[63] and in misoriented graphene bilayers [64]. In addition to these system twisted 2D moiré patterns have also been observed in surface
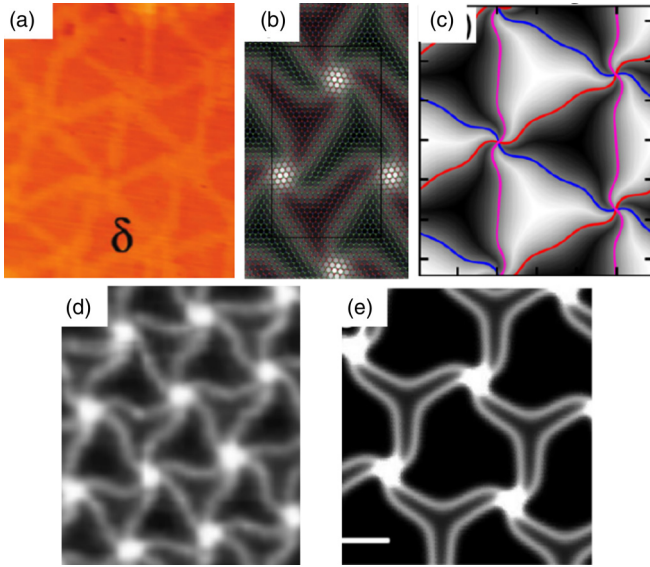
FIG. 24. Experimental evidence for twisted states in microscopy images. (a) TiO$_x$ on Au(111) taken from Ref. [61] (also observed by Tumino *et al.*[62]). (b) Ag on Ru(0001) taken from Ref. [63] where the system was numerically relaxed with a Frenkel-Kontorova model with an initial condition provided by the experiments. (c) Patterns observed in misoriented graphene bilayers taken from Ref. [64]. (d) Surface reconstruction of Au(111) after exposing the surface to Gd for approximately 20 s, taken from Ref. [65]. (e) Surface reconstruction of Pt (111) after additional density added to surface, taken from Ref. [66].

reconstruction experiments on Au(111) exposed to Gd, and simulations of Pt(111) surfaces with excess density. While most of these systems may not be compatible with the 2D model systems considered in this work, where the substrate is approximated by a simple rigid adsorption potential, the basic underlying cause of formation of the twisted state is likely the same. The relative symmetry of the film or surface compared to the bulk state gives rise to a triangular network of domain walls with the junctions in very high potentially energy locations. Energy can be released by twisting the junctions such that the surface atoms move slightly away from the potential maxima, giving rise to the twisted 2D moiré state.

VII. LIMITATIONS OF MODELING

The approach proposed in this work is perhaps the simplest method that incorporates elasticity, crystal symmetries, and dislocations on the long length and time scales needed to study surface ordering. It is also clear that the approach does not include many physical features that could influence the strain-induced patterning. Two obvious limitations are the lack of out of plane deformations and approximating the substrate as a rigid periodic potential with the simplest lowest order harmonics. In the former case it is likely that the deformations will play a role at defects, such as domain walls and junctions. In the latter case substrate relaxation may play a role if the substrate-film coupling is strong as would be the case for metal-on-metal systems, but may not be as important in graphene or hexagonal boron nitride on metallic surfaces since

the coupling is relatively weak in most cases (Cu and Ni being the exceptions [46]).

Another important feature that was not included in this work is the influence of thermal fluctuations. It is well known that they play an important role in determining the order of the phase transitions. It is quite likely that the characteristics of the mean field phase transitions discussed in this work will be altered by the inclusion of thermal fluctuations. While it is relatively straightforward to include such fluctuations in the amplitude expansion approach (see, for example, Huang *et al.*[53]) or in the original PFC model [67,68], it maybe computationally challenging to examine all the transitions discussed in this manuscript. In particular, an interesting question is whether or not a liquid phase can intervene between the commensurate and incommensurate phases due to thermally induced dislocation pairs [69].

In principle, the limitations discussed in the previous paragraphs could be incorporated into the methodology presented in this work. However, there are some other effects that are much more diffcult to model using this technique. It can be difficult to incorporate higher order harmonics and to model the very large deformation limit. The former case is possible, however, the computational cost can be quite significant. In the latter case the amplitude expansion explicitly breaks down in the limit that the amplitude varying on too small length scales, which occurs in this limit. Clearly when the size of the patterns becomes very small this becomes a problem.

VIII. SUMMARY AND CONCLUSIONS

The modeling approach used in this manuscript as described by the simple complex amplitude approach [i.e., the free functional given in Eq. (15)], while perhaps missing some features, provides a basis for examining a broad class of systems with relative computational ease. Compared to quantum mechanical density functional theory, molecular dynamics, or even the relatively simple Frenkel-Kontorova model, this method can examine systems orders magnitude larger on much longer time scales. In this manuscript phase diagrams were computed in the mean field limit for five different systems (in addition to three others previously considered) illustrating the power of the approach.

While there are many possible physical features that could be added to the existing approach, perhaps the most interesting extension would be films that contain more than one type of atom. Of specific interest in recent years are 2D films such as hexagonal boron nitrite (hBN), molybdenum disulfide, and other transition metal dichalcogenides which are distinctly different from graphene and have many potential applications. It would be very interesting to see how, for example, inversion boundaries in these systems can be used to relieve strain and potential lead to different patterns, such as the pinwheel type structure delineated by inversion boundaries as observed in hBN [70].

---

[1] A. K. Geim and K. S. Novoselov, Nat. Mater. **6**, 183 (2007).

[2] K. S. Novoselov, V. I. Fal, L. Colombo, P. R. Gellert, M. G. Schwab, and K. Kim, Nature **490**, 192 (2012).

[3] P. P. Merino, M. Svec, A. L. Pinardi, G. Otero, and J. A. Martin-Gago, ACS Nano **5**, 5627 (2011).

[4] P. Sule, M. Szendro, C. Hwang, and L. Tapaszto, Carbon **77**, 1082 (2014).

[5] P. Sutter, J. T. Sadowski, and E. Sutter, Phys. Rev. B **80**, 245411 (2009).

[6] X. Li, W. Cai, J. An, S. Kim, J. Nah, D. Yang, R. Piner, A. Velamakanni, I. Jung, E. Tutuc, S. K. Banerjee, L. Colombo, and R. S. Ruoff, Science **324**, 1312 (2009).

[7] R. Grantab, V. B. Shenoy, and R. S. Ruoff, Science **330**, 946 (2010).

[8] J. F. Gao, J. Yip, J. J. Zhao, B. I. Yakobson, and F. Ding, J. Am. Chem. Soc. **133**, 5009 (2011).

[9] Z. Sun, S. K. Hamalainen, J. Sainio, J. Lahtinen, D. Vanmaekelbergh, and P. Liljeroth, Phys. Rev. B **83**, 081415(R) (2011).

[10] S. Marchini, S. Günther, and J. Wintterlin, Phys. Rev. B **76**, 075429 (2007).

[11] K. R. Elder, Z. Chen, K. L. M. Elder, P. Hirvonen, S. K. Mkhonta, S.-C. Ying, E. Granato, Z.-F. Huang, and T. Ala-Nissila, J. Chem. Phys. **144**, 174703 (2016).

[12] F. Schulz, R. Drost, S. K. Hämäläinen, T. Demonchaux, A. P. Seitsonen, and P. Liljeroth, Phys. Rev. B **89**, 235429 (2014).

[13] S. Joshi, D. Ecija, R. Koitz, M. Iannuzzi, A. P. Seitsonen, J. Hutter, H. Sachdev, S. Vijayaraghavan, F. Bischoff, K. Seufert, J. V. Barth, and W. Auwaerter, Nano Lett. **12**, 5821 (2012).

[14] S. Joshi, F. Bischoff, R. Koitz, D. Ecija, K. Seufert, A. P. Seitsonen, J. Hutter, K. Diller, J. I. Urgel, H. Sachdev, J. V. Barth, and W. Auwärter, ACS Nano **8**, 430 (2014).

[15] A. Preobrajenski, A. Vinogradov, and N. Martensson, Surf. Sci. **582**, 21 (2005).

[16] M. Corso, W. Auwärter, M. Muntwiler, A. Tamai, T. Greber, and J. Osterwalder, Science **303**, 217 (2004).

[17] S. Berner, M. Corso, R. Widmer, O. Groening, R. Laskowski, P. Blaha, K. Schwarz, A. Goriachko, H. Over, S. Gsell, M. Schreck, H. Sachdev, T. Greber, and J. Osterwalder, Angew. Chem. Int. Ed. **46**, 5115 (2007).

[18] J. G. Diaz, Y. Ding, R. Koitz, A. P. Seitsonen, M. Iannuzzi, and J. Hutter, Theor. Chem. Acc. **132**, 1350 (2013).

[19] A. Goriachko, Y. He, M. Knapp, H. Over, M. Corso, T. Brugger, S. Berner, J. Osterwalder, and T. Greber, Langmuir **23**, 2928 (2007).

[20] C. F. Castro-Guerrero, F. L. Deepak, A. Ponce, J. Cruz-Reyes, M. D. Valle-Granados, S. Fuentes-Moyado, D. H. Galvan, and M. Jose-Yacaman, Catal. Sci. Technol. **1**, 1024 (2011).

[21] H. C. Daz, R. Addou, and M. Batzill, Nanoscale **6**, 1071 (2014).

[22] J. Jeon, S. K. Jang, S. M. Jeon, G. Yoo, Y. H. Jang, J.-H. Park, and S. Lee, Nanoscale **7**, 1688 (2015).

[23] C. Gunther, J. Vrijmoeth, R. Q. Hwang, and R. J. Behm, Phys. Rev. Lett. **74**, 754 (1995).

[24] K. R. Elder, G. Rossi, P. Kanerva, F. Sanches, S.-C. Ying, E. Granato, C. V. Achim, and T. Ala-Nissila, Phys. Rev. Lett. **108**, 226102 (2012).

[25] K. R. Elder, G. Rossi, P. Kanerva, F. Sanches, S.-C. Ying, E. Granato, C. V. Achim, and T. Ala-Nissila, Phys. Rev. B **88**, 075423 (2013).

[26] F. E. Gabaly, W. L. W. Ling, K. F. McCarty, and J. de la Figuera, Science **308**, 1303 (2005).

[27] A. K. Schmid, N. C. Bartelt, J. C. Hamilton, C. B. Carter, and R. Q. Hwang, Phys. Rev. Lett. **78**, 3507 (1997).

[28] S.-F. Ding, S.-R. Deng, H.-S. Lu, Y.-L. Jiang, G.-P. Ru, D. W. Zhang, and X.-P. Qu, J. Appl. Phys. **107**, 103534 (2010).

[29] A. Wander, C. J. Barnes, L. D. Mapledoram, and D. A. King, Surf. Sci. **281**, 42 (1993).

[30] M. Wasniowska, W. Wulfhekel, M. Przybylski, and J. Kirschner, Phys. Rev. B **78**, 035405 (2008).

[31] J. Jalkanen, G. Rossi, O. Trushin, E. Granato, T. Ala-Nissila, and S.-C. Ying, Phys. Rev. B **81**, 041412 (2010).

[32] W. E. McMahon, E. S. Hirschhorn, and T.-C. Chiang, Surf. Sci. Lett. **279**, L231 (1992).

[33] I. Meunier, G. Treglia, J. M. Gay, B. Aufray, and B. Legrand, Phys. Rev. B **59**, 10910 (1999).

[34] K. Umezawa, S. Nakanishi, M. Yoshimura, K. Ojima, K. Ueda, and W. M. Gibson, Phys. Rev. B **63**, 035402 (2000).

[35] A. Bendounan, H. Cercellier, Y. Fagot-Revurat, B. Kierren, V. Y. Yurov, and D. Malterre, Appl. Surf. Sci **212**, 33 (2003).

[36] A. Bendounan, H. Cercellier, B. Kierren, Y. Fagot-Revurat, V. Y. Yurov, and D. Malterre, Europhys. Lett. **64**, 392 (2003).

[37] D. Malterre, B. Kierren, Y. Fagot-Revurat, C. Didiot, F. J. G. de Abajo, F. Schiller, J. Cordon, and J. E. Ortega, New J. Phys. **13**, 013026 (2011).

[38] F. Schiller, J. Cordon, D. Vyalikh, A. Rubio, and J. E. Ortega, Phys. Rev. Lett. **94**, 016103 (2005).

[39] J. Jacobsen, L. P. Nielsen, F. Besenbacher, I. Stensgaard, E. Laegsgaard, T. Rasmussen, K. W. Jacobsen, and J. K. Norskov, Phys. Rev. Lett. **75**, 489 (1995).

[40] J. Suzanne and J. M. Gay, in *Physical Structure—Handbook of Surface Science*, edited by W. N. Unertl (North-Holland, Amsterdam, 1996), Vol. 1, Chap. 10, The Structure of Physically Adsorbed Phases, p. 503.

[41] E. D. Specht, A. Mak, C. Peters, M. Sutton, R. J. Birgeneau, K. L. D'Amico, D. E. Moncton, S. E. Nagler, and P. M. Horn, Z. Phys. B **69**, 347 (1987).

[42] K. Kern, R. David, P. Zeppenfeld, and G. Comsa, Surf. Sci. **195**, 353 (1988).

[43] Y. G. Ding, C. T. Chan, and K. M. Ho, Phys. Rev. Lett. **67**, 1454 (1991).

[44] H. Over, C. P. Wang, and F. Jona, Phys. Rev. B **51**, 4231 (1995).

[45] C. Stampfl, J. Burchhardt, M. Nielsen, D. L. Adams, M. Scheffler, H. Over, and W. Moritz, Surf. Sci. **287**, 418 (1993).

[46] M. Smirman, D. Taha, A. K. Singh, Z.-F. Huang, and K. R. Elder, Phys. Rev. B **95**, 085407 (2017).

[47] K. R. Elder, C. Achim, E. Granato, S. Ying, and T. Ala-Nissila, Europhys. Lett. **116**, 56002 (2016).

[48] N. Goldenfeld, B. P. Athreya, and J. A. Dantzig, Phys. Rev. E **72**, 020601 (2005).

[49] B. P. Athreya, N. Goldenfeld, and J. A. Dantzig, Phys. Rev. E **74**, 011601 (2006).

[50] B. P. Athreya, N. Goldenfeld, J. A. Dantzig, M. Greenwood, and N. Provatas, Phys. Rev. E **76**, 056706 (2007).

[51] D.-H. Yeon, Z.-F. Huang, K. R. Elder, and K. Thornton, Phil. Mag. **90**, 237 (2010).

[52] K. R. Elder, Z.-F. Huang, and N. Provatas, Phys. Rev. E **81**, 011602 (2010).

[53] Z.-F. Huang, K. R. Elder, and N. Provatas, Phys. Rev. E **82**, 021605 (2010).

[54] K. R. Elder, M. Katakowski, M. Haataja, and M. Grant, Phys. Rev. Lett. **88**, 245701 (2002).

[55] K. R. Elder and M. Grant, Phys. Rev. E **70**, 051605 (2004).

[56] K. R. Elder, N. Provatas, J. Berry, P. Stefanovic, and M. Grant, Phys. Rev. B **75**, 064107 (2007).

[57] A. Jaatinen, C. V. Achim, K. R. Elder, and T. Ala-Nissila, Phys. Rev. E **80**, 031602 (2009).

[58] P. M. Chaikin and T. C. Lubensky, *Principles of Condensed Matter Physics* (Cambridge University Press, Cambridge, England, 1995).

[59] A. Dahal and M. Batzill, Nanoscale **6**, 2548 (2014).

[60] D. Usachov, A. M. Dobrotvorskii, A. Varykhalov, O. Rader, W. Gudat, A. M. Shikin, and V. K. Adamchuk, Phys. Rev. B **78**, 085403 (2008).

[61] C. Wu, M. S. J. Marshall, and M. R. Castell, J. Phys. Chem. C **115**, 8643 (2011).

[62] F. Tumino, P. Carrozzo, L. Mascaretti, C. S. Casari, M. Passoni, S. Tosoni, C. E. Bottani, and A. L. Bassi, 2D Mater. **2**, 045011 (2015).

[63] W. L. Ling, J. C. Hamilton, K. Thurmer, G. E. Thayer, J. de la Figuera, R. Q. Hwang, C. B. Carter, N. C. Bartelt, and K. F. McCarty, Surf. Sci. **600**, 1735 (2006).

[64] S. Dai, Y. Xiang, and D. J. Srolovitz, Nano Lett. **16**, 5923 (2016).

[65] M. Corso, L. Fernández, F. Schiller, and J. E. Ortega, ACS Nano **4**, 1603 (2010).

[66] R. Pushpa and S. Narasimhan, Phys. Rev. B **67**, 205418 (2003).

[67] J. A. P. Ramos, E. Granato, C. V. Achim, S. C. Ying, K. R. Elder, and T. Ala-Nissila, Phys. Rev. E **78**, 031109 (2008).

[68] J. A. P. Ramos, E. Granato, S. C. Ying, C. V. Achim, K. R. Elder, and T. Ala-Nissila, Phys. Rev. E **81**, 011121 (2010).

[69] S. N. Coppersmith, D. S. Fisher, B. I. Halperin, P. A. Lee, and W. F. Brinkman, Phys. Rev. Lett. **46**, 549 (1981).

[70] H. Liu, L. Jiao, F. Yang, Y. Cai, X. Wu, W. Ho, C. Gao, J. Jia, N. Wang, H. Fan, W. Yao, and M. Xie, Phys. Rev. Lett. **113**, 066105 (2014).